GEOPHYSICS, VOL. 91, NO. 1 (JANUARY-FEBRUARY 2026); P. WA35–WA46, 17 FIGS., 7 TABLES.
10.1190/GEO2025-0175.1

Deep neural networks for estimating S-wave velocity in tight sandstone reservoirs from log data

Zhijian Fang[1], Jing Ba[2], José M Carcione[3], Fansheng Xiong[4], Qiang Guo[5], and Wei Cheng[6]

ABSTRACT

Accurate estimation of S-wave velocity from well logs is relevant for processing seismic data from hydrocarbon reservoirs, CO_2 storage sites, and geothermal systems. Standard methods rely on empirical relationships and basic rock-physics models (RPMs), such as the Gassmann equation, which are often inaccurate because they cannot account for the complex factors that influence the relationship between S-wave velocity and other properties. Machine-learning techniques, such as deep neural networks (DNNs), have been shown to be effective methods for the indirect estimation of S-wave logs and other rock properties. In this work, we develop a novel prediction method that combines RPMs (Xu-White and Biot-Rayleigh [BR] models) and DNNs based on pseudolabels, i.e., a class of algorithms that use model outputs to assign labels to unlabeled samples, which are then used as labeled samples during training. The BR model takes into account the volume ratio of inclusions and treats it as a spatially varying parameter, allowing for a better description of the pore microstructure. Data from five boreholes demonstrate the applicability of our model. A single well is used for training, and the remaining four wells are used as a blind test. Compared with DNNs without physical poroelasticity models, the method driven by models indicates a significant improvement in prediction accuracy. By incorporating pseudolabels into the BR model, the prediction performance of the network model is improved. The method proposed in this work is validated and applied in other work areas.

INTRODUCTION

Given the demand for hydrocarbons during the global energy transition period, tight sandstones have attracted increasing attention in recent decades (Ba et al., 2023a, 2023b; Zhang et al., 2023). These unconventional reservoirs play a crucial role in meeting energy needs while lower-carbon alternatives are being developed (Zou et al., 2012; Kadkhodaie and Kadkhodaie, 2022; Jia et al., 2023; Sambo et al., 2023; Kocoglu et al., 2024; Evro et al., 2025). In tight sandstone reservoirs, the mineral composition, cement types, and their volumes vary considerably, resulting in an uneven spatial distribution of the rock mechanical and elastic properties. In addition, pore types are diverse, and pore sizes and connectivity show remarkable variations. This strong heterogeneity increases the uncertainty in the prediction and evaluation of reservoirs (Dautriat et al., 2011; Guo and Fu, 2024; Guo et al., 2024; Pan et al., 2024; Brantut and Baud, 2025).

Wellbore S-wave velocity, together with other rock properties, plays a key role in the field of geophysical exploration, i.e., forward seismic modeling and inversion, fluid and lithology identification, and reservoir stress analysis, especially in tight sandstone reservoirs (Lee, 2006; Dumke and Berndt, 2019; Oloruntobi and Butt, 2020; Zhao et al., 2020). In addition to conventional hydrocarbon applications, S-wave velocity has emerged as a critical parameter for carbon capture and storage projects (Agofack et al., 2018; Carcione et al., 2023; Khalilidermani and Knez, 2024). It enables a quanti-

Manuscript received by the Editor 12 March 2025; revised manuscript received 29 May 2025; published ahead of production 9 July 2025; published online 26 November 2025.
[1]Hohai University, School of Earth Sciences and Engineering, Nanjing, China and University of Lausanne, Institute of Earth Sciences, Lausanne, Switzerland. E-mail: zhijian.fang@unil.ch.
[2]Hohai University, School of Earth Sciences and Engineering, Nanjing, China. E-mail: jba@hhu.edu.cn (corresponding author).
[3]Hohai University, School of Earth Sciences and Engineering, Nanjing, China and National Institute of Oceanography and Applied Geophysics — OGS, Trieste, Italy. E-mail: jose.carcione@gmail.com.
[4]Beijing Institute of Mathematical Sciences and Applications, Beijing, China. E-mail: fansheng_xiong@bimsa.cn.
[5]China University of Mining and Technology, School of Resources and Geosciences, Xuzhou, China. E-mail: qiangguo@cumt.edu.cn.
[6]SINOPEC Geophysical Research Institute Co., Ltd., Nanjing, China. E-mail: chengwei21@foxmail.com.

tative assessment of the caprock sealing efficiency through dynamic mechanical property analysis (the ratio of the P- to S-wave velocity and Young's modulus), monitors CO_2 plume migration via time-lapse velocity changes, and optimizes storage capacity estimation through fluid substitution modeling (Kim et al., 2011; Ivanova et al., 2012; Ajo-Franklin et al., 2013; Khatiwada et al., 2013). However, due to various factors, such as well conditions, logging tools, high acquisition costs, and incomplete measurements in old wells, S-wave logs are often not available (Rezaee et al., 2007; Wang and Cao, 2021; Feng et al., 2024; Zhao et al., 2024), making their estimation essential.

In the absence of S-wave velocity (V_S) data in well logging, extensive prediction methods have been conducted. These conventional approaches can be divided into two categories: empirical equations and rock-physics models (RPMs). Empirical equations are primarily established by determining the relationship between V_S and other rock-physics properties (e.g., P-wave velocity [V_P] and density) through experiments or well-logging data (Mavko et al., 2020). For instance, Wilkens et al. (1984), Han et al. (1986), and Qin et al. (2022) measure the V_P and V_S of rock samples in the laboratory and establish an empirical equation between these two quantities to predict V_S. This approach demands a large amount of data and is highly susceptible to regional variations, horizontal and vertical, which may negatively impact prediction accuracy. In contrast, RPMs are more reliable, with the most widely used RPM being of the Xu-White model (Xu and White, 1995, 1996). Following the Xu-White model, several improved RPMs have been proposed to predict V_S in different reservoirs

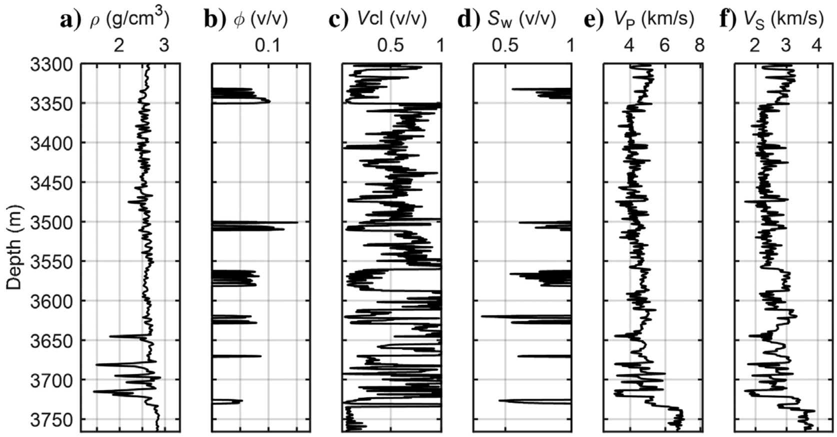

Figure 1. Log data of (a) the density, (b) porosity, (c) clay volume, (d) water saturation, (e) P-wave velocity, and (f) S-wave velocity from well 1.

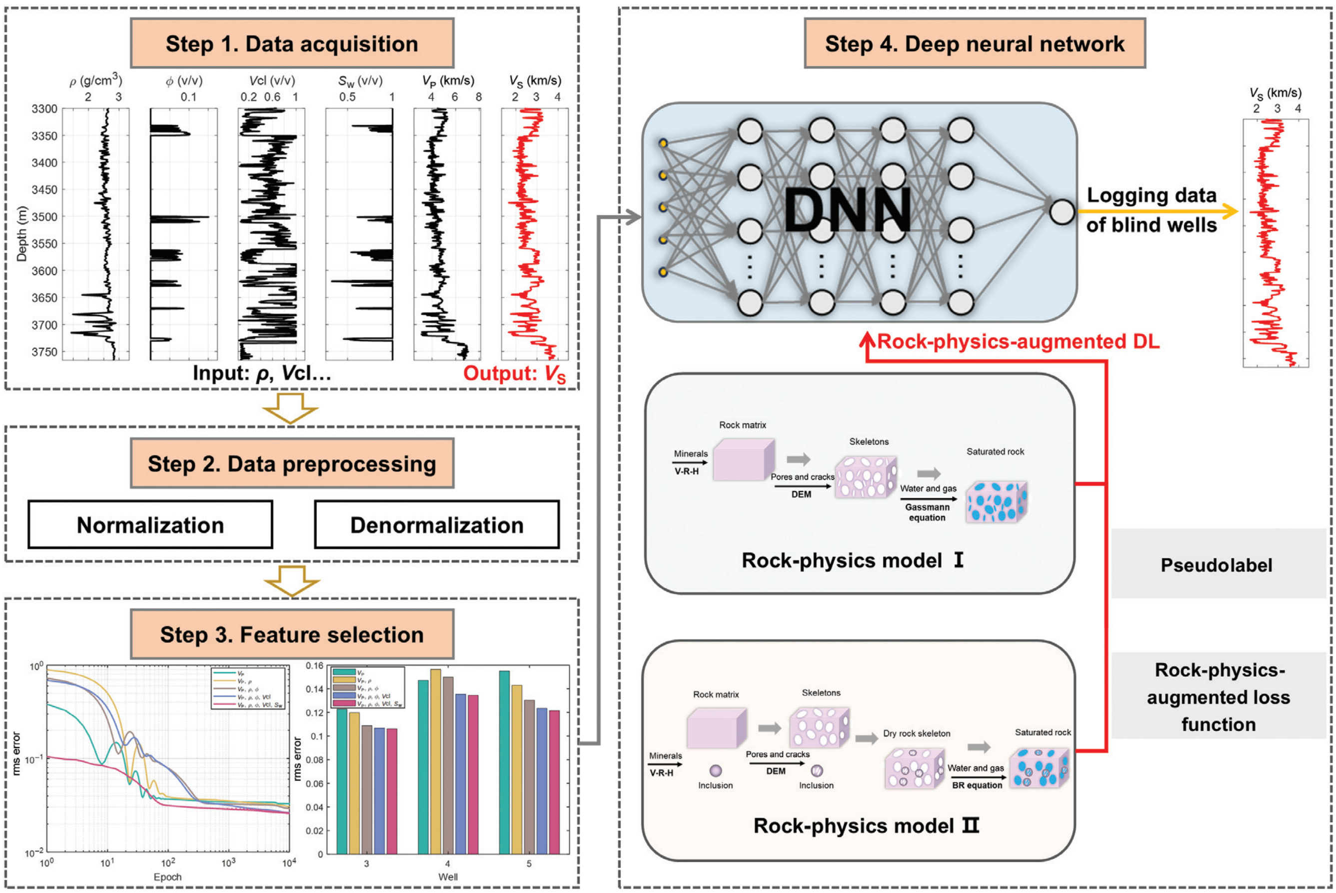

Figure 2. Workflow for the RPM-driven DNN.

(Carcione et al., 2011; Guo and Li, 2015; Wang et al., 2019; Fang et al., 2022, 2024). However, these S-wave predictions have been performed by assuming simple pore structures, and these models do not account for microheterogeneities and fluid patches as do more complex theories, for instance, the Biot-Rayleigh (BR) poroelasticity model (Ba et al., 2011, 2017).

With the use of big data and machine-learning (ML) methods, deep neural networks (DNNs) have become popular for predicting reservoir properties from borehole data. By training network models with large data sets, the relationship between well data and reservoir properties can be effectively mapped (Rajabi et al., 2010; Anemangely et al., 2017; Qadrouh et al., 2019; You et al., 2020, 2021; Xiong et al., 2021; Zou et al., 2021; Li et al., 2023). Previous researchers have conducted extensive studies on the prediction of reservoir properties and have made significant progress. For example, using well data, Zhang et al. (2018) show that well logs synthesized using long short-term memory (LSTM) are more accurate and better suited for complex problems than those generated by fully connected neural networks. Gu et al. (2019) develop a hybrid data-driven model by using particle swarm optimization (PSO) and support vector machines (SVMs), which shows excellent performance in permeability prediction. In particular, various ML techniques are used to predict the V_S data, such as gated recurrent units, artificial neural networks, LSTM, PSO, and SVM (Bagheripour et al., 2015; Singh et al., 2015; Anemangely et al., 2019; Wang and Cao, 2021; Jiang et al., 2022; Yang et al., 2023; Zhao et al., 2024). Compared with traditional ML methods, DNNs possess an inherent capability to hierarchically extract discriminative features directly from the raw input data, eliminating the need for manual feature engineering through their end-to-end learning paradigm. This representation learning capacity enables DNNs to not only discover complicated latent patterns within high-dimensional data spaces but also to exhibit robust generalization performance when applied to previously unknown data sets, as evidenced by their superior performance in various ML benchmarks. Most methods for predicting V_S using ML primarily focus on improving the prediction accuracy of reservoir properties through model type selection, structural adjustments, parameter settings, and data processing. However, they often overlook the potential improvement in prediction accuracy that could be achieved by considering the correlations between reservoir properties (Fang et al., 2024). In addition, the traditional ML-based method for V_S prediction faces challenges due to limited generalization and insufficiently labeled data for building predictive models, making it difficult to implement in practice (Feng et al., 2024).

This work aims to improve the accuracy of V_S prediction by using RPM-driven DNN approaches. To validate the effectiveness of the proposed methodology in a practical scenario, we train the neural network (NN) model using data from one well and subsequently assess its performance on the remaining wells within the tight sandstones of the Ordos Basin. Two RPMs (the Xu-White and BR models) for V_S estimation, which incorporate more potential physical information, serve as physical constraints in the process of DNN training. In particular, when modeling is based on the BR equation,

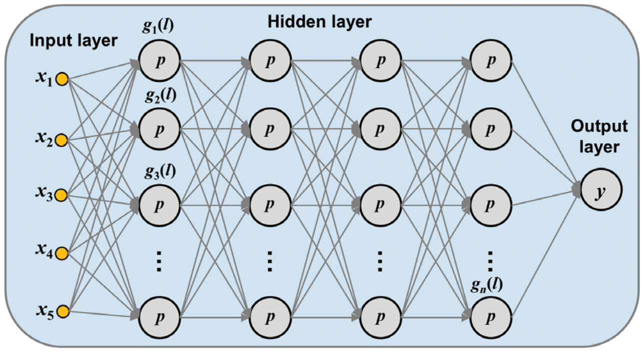

Figure 3. Deep neural network.

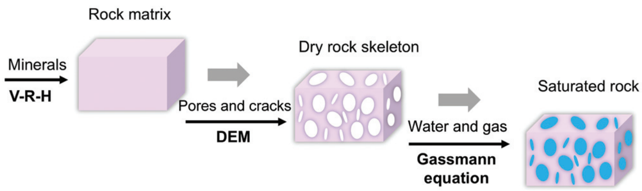

Figure 4. Workflow of the Xu-White model.

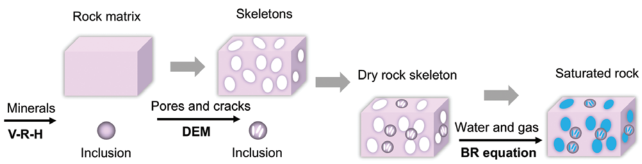

Figure 5. Workflow of the BR model.

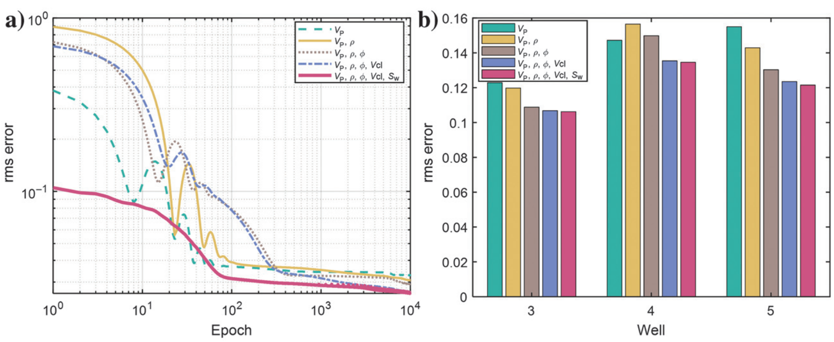

Figure 6. (a) The loss function curves of a DNN model and (b) the RMSE of different parameter group inputs used in training the DNN model.

Table 1. The prediction accuracy of different feature combinations.

Number of input feature (s)	Selected input feature (s)	Average RMSE
1	V_P	0.1417
2	V_P, ρ	0.1397
3	V_P, ρ, ϕ	0.1296
4	V_P, ρ, ϕ, Vcl	0.1219
5	V_P, ρ, ϕ, Vcl, S_w	0.1207

we consider the inclusion volume with spatial variations to describe the rock heterogeneities. Finally, the proposed method is validated and applied in other areas.

Table 2. Rock properties for the Xu-White and BR models (Mavko et al., 2020).

Property	Symbol	Value and unit
Quartz bulk modulus	K_{quartz}	37 GPa
Clay bulk modulus	K_{clay}	21 GPa
Feldspar bulk modulus	K_{feldspar}	37.5 GPa
Water bulk modulus	K_{water}	2.34 GPa
Gas bulk modulus	K_{gas}	0.081 GPa
Quartz shear modulus	μ_{quartz}	44 GPa
Clay shear modulus	μ_{clay}	7 GPa
Feldspar shear modulus	μ_{feldspar}	15 GPa
Quartz density	ρ_{quartz}	2.65 g/cm^3
Clay density	ρ_{clay}	2.60 g/cm^3
Feldspar density	ρ_{feldspar}	2.62 g/cm^3
Water density	ρ_{water}	0.945 g/cm^3
Gas density	ρ_{gas}	0.204 g/cm^3
Aspect ratio of pores	α_{s}	0.12
Aspect ratio of cracks	α_{c}	0.035
Radius of inclusion	R_0	0.05 m
Angular frequency	ω	100π rad/s
Viscosity of fluid	η	0.001 Pa·s

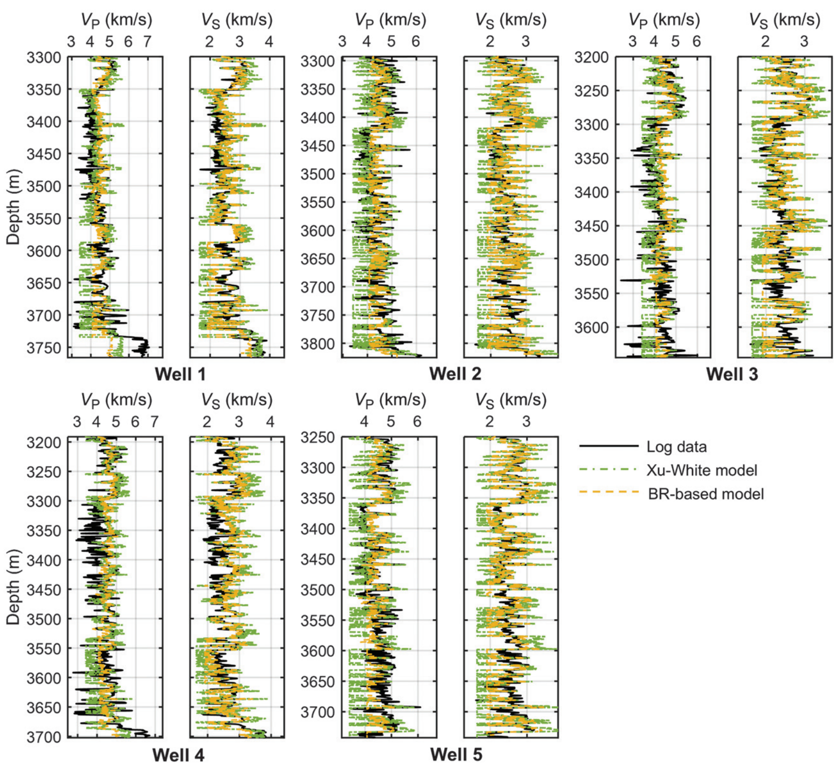

Figure 7. The predicted V_{P} and V_{S} obtained by using the Xu-White and BR models.

GEOLOGY AND DATA

The reservoir

The structural features of the Ordos Basin are generally considered to be an asymmetric, dustpan-shaped syncline that is gentle in the east and steep in the west. Based on bedrock characteristics, structural attributes, and geologic evolution history, the Ordos Basin can be subdivided into six structural units. The study area in this work is situated within the Shanbei Slope structural unit, located in the northern central region of the basin. This unit is characterized by a monocline structure, covering an area of approximately 900 km^2. The area is marked by several rows of low amplitude, gently sloping elevations that extend across the slope in a northeast-to-southwest orientation.

Data preparation

The data set consists of borehole measurements made at five boreholes in the study region. After data preprocessing, we obtain 19,581 data points suitable for training and testing, covering all required variables. The number of data points varies across different wells. To evaluate the DNN model performance, wells 3, 4, and 5 are selected as a test data set. Wells 1 and 2 (7989 data points in total) are used for training the DNN model. Figure 1 shows the data from well 1, including density (ρ), porosity (ϕ), clay volume (Vcl), water saturation (S_{w}), and P- and S-wave velocities (V_{P} and V_{S}, respectively).

METHODOLOGY

Workflow

The aim of this work is to predict the V_{S} in tight sandstone reservoirs by using the proposed RPM-driven DNN approach. Figure 2 shows the workflow. First, the collected data are preprocessed by removing the outliers. Because the magnitudes of the different parameters vary, normalization is required before the data are entered into the DNN model, as this facilitates the convergence of the NN and increases stability. Feature selection is required to determine the optimal combination of input parameters. After feature selection, the measured data, i.e., ρ, ϕ, Vcl, S_{w}, and V_{P}, are used as inputs, whereas V_{S} is used as the output. A DNN is then used to train the model. We integrate the Xu-White and BR models into the DNN. We implement several physics-driven DNN strategies, such as constructing pseudolabels and using an RPM-driven loss function.

Deep neural networks

DNNs consist of several layers, usually an input layer, one or more hidden layers, and an output layer, as shown in Figure 3. The input layer consists of neurons corresponding to the number of input features, whereas the output layer contains neurons representing the number of outputs to be predicted. Hidden layers, which may consist of multiple layers and neurons, process the outputs of the previous layer and pass them on as inputs to the subsequent layer to enable feature mapping (e.g., Qadrouh et al., 2019). This mapping is achieved by a combination of a linear transformation within each neuron and a nonlinear activation function.

Poroelasticity models

RPMs are used to derive V_P and V_S based on mineral composition, pore geometry, porosity, and fluid type. In this study, the Xu-White and BR models are primarily used to generate pseudolabels, which, in combination with additional features, expand the information available for network training and improve the generalization capability of the model. These pseudolabels are integrated into the network together with the original well attributes to facilitate model training.

Xu-White model

The Xu-White model introduced by Xu and White (1995) is used to predict the elastic properties of fluid-saturated media. It consists of three main steps: (1) estimating the elastic moduli of the rock matrix and fluids, (2) calculating the elastic moduli of the dry rock, and (3) performing fluid substitution. The workflow of the Xu-White model is shown in Figure 4. First, the elastic properties of the mineral mixture are determined using the Voigt-Reuss-Hill average. Then, the elastic moduli of the dry rock are derived by including the pores and cracks in the matrix using the differential effective medium (DEM) model (Mavko et al., 2020). Later, the elastic properties of the wet rock are calculated using Gassmann's equation (Gassmann, 1951). Finally, the V_S is determined from the shear modulus and density of the rock. In addition, the fluid mixture's bulk modulus (consisting of gas and water) is determined using the Wood equation.

BR model

The BR model (Ba et al., 2011) considers the rock as a double-porosity medium, characterized by spherical inclusions embedded within an unbounded host medium, each exhibiting distinct porosities and pore structures. The governing equations for this model are provided in Appendix A. Unlike traditional RPMs, such as Gassmann's model, which rely on homogeneous assumptions, the BR model explicitly accounts for heterogeneities resulting from variations in mineral composition and pore geometry. The workflow of the BR modeling is shown in Figure 5. The dry-rock moduli are first derived using the DEM method, followed by fluid substitution. In contrast to the process shown in Figure 4, the BR model treats the matrix as a composite of the embedded inclusions and the host medium, both consisting of solid grains and pores. We compute a plane-wave analysis of the BR differential equations to obtain the P-wave phase velocity (see equations A-1–A-8). The S-wave velocity is estimated using the shear modulus of the skeleton and the density of the fluid-saturated rock. The fluid mixture's bulk modulus is determined using the Wood equation.

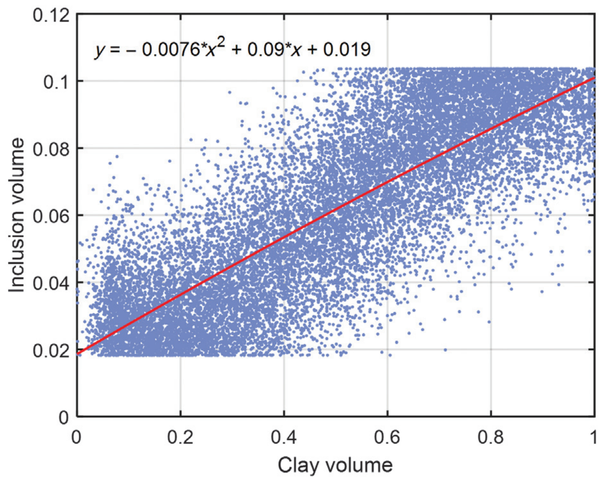

Figure 8. The empirical relationship between the inclusion and clay volume.

Table 3. Sampling ranges for the rock properties.

Property	Symbol (unit)	Lower bound	Upper bound
Density	ρ (g/cm^3)	1.5	3
Porosity	ϕ (v/v)	0.001	0.15
Clay volume	Vcl (v/v)	0.01	0.99
Water saturation	S_w (v/v)	0.01	0.99

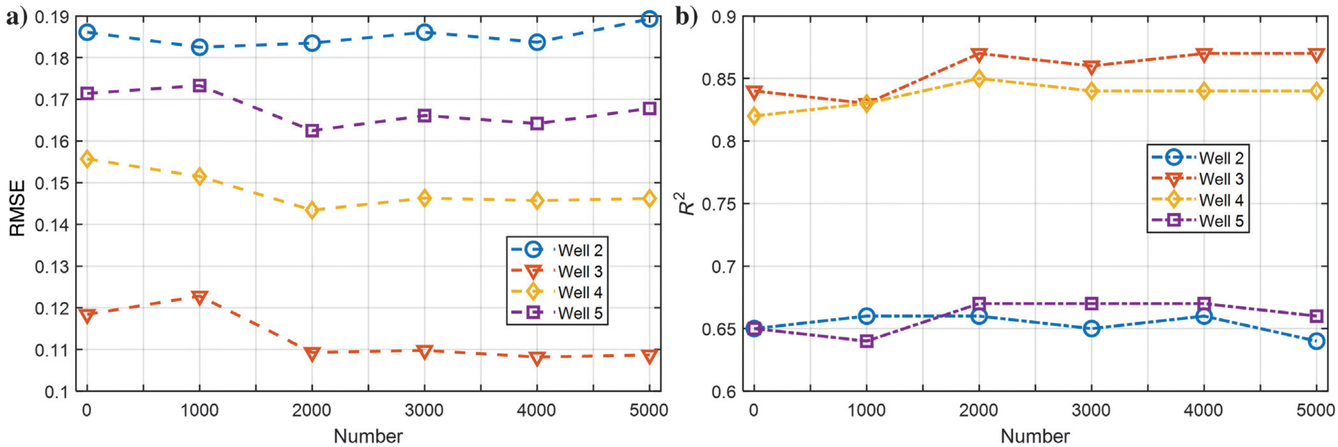

Figure 9. Prediction accuracies of the V_S for different pseudolabel data volumes: (a) RMSE and (b) R^2.

In complex reservoirs, the pore structure and mineral composition distribution are heterogeneous. The BR model addresses this problem by modeling the rock as a medium containing spherical inclusions with a low volume fraction v_c within a host medium of higher volume fraction v_h. The total rock porosity ϕ is given by $\phi = \phi_{10}v_h + \phi_{20}v_c$ and $v_h + v_c = 1$. Here, ϕ_{10} and ϕ_{20} correspond to the porosities of the host and inclusion components, respectively. To account for fabric heterogeneities, the inclusion volume v is treated as a depth-dependent variable. This variable is derived by matching the predicted wave velocities ($V_P^{\mathrm{cal}}, V_S^{\mathrm{cal}}$) to the real log wave velocities ($V_P^{\mathrm{real}}, V_S^{\mathrm{real}}$) during the well-log calibration process as follows:

$$\hat{\mathbf{v}} = \arg\min\left(\frac{1}{2}\times(\|V_P^{\mathrm{cal}}(\mathbf{v}) - V_P^{\mathrm{real}}\|_2 + \|V_S^{\mathrm{cal}}(\mathbf{v}) - V_S^{\mathrm{real}}\|_2)\right), \tag{1}$$

where $\mathbf{v} = [v_{c1}, v_{c2}, \ldots, v_{cj}]^T$ with j representing the sample number in the well.

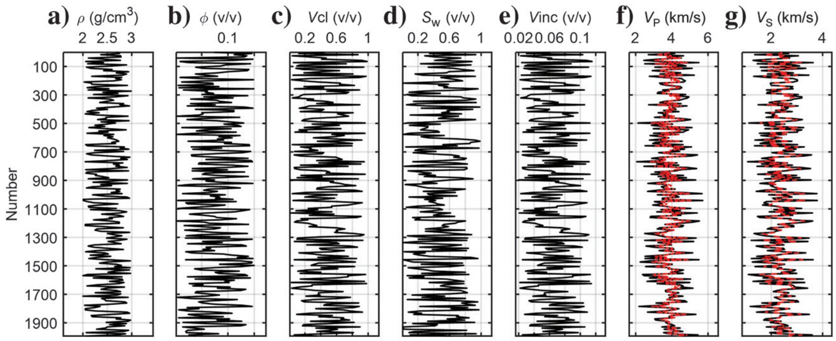

Figure 10. The calculated V_P and V_S of the pseudolabels using the Xu-White model (the black curve) and the BR model (the red curve).

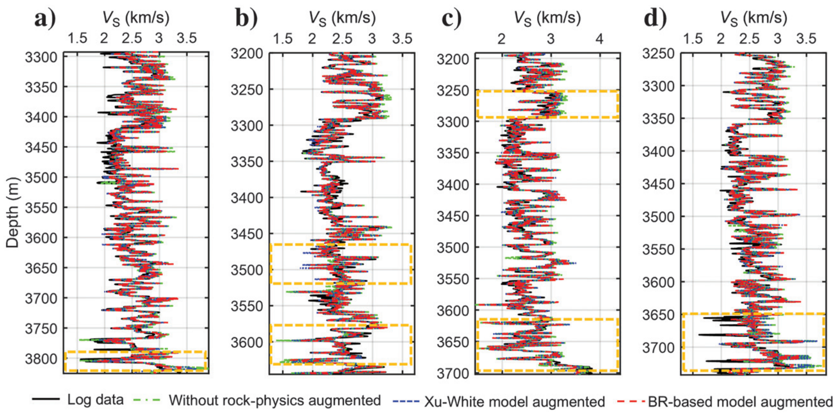

Figure 11. Comparisons of the DNN test for V_S prediction by using the Xu-White and BR models for well 1 training.

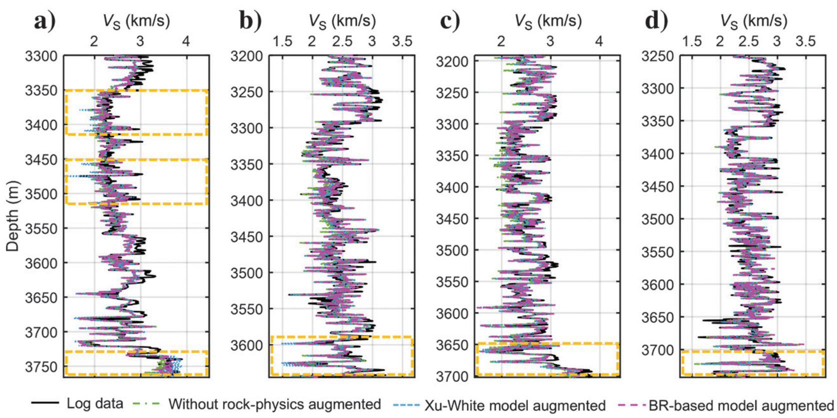

Figure 12. Comparisons of the DNN test for V_S prediction by using the Xu-White and BR models for well 2 training.

Loss function

The loss function quantifies the deviation between the predicted and real results, guiding the NN to optimize its parameters accordingly. In this study, the mean-squared error is used to define the physically driven loss function. Initially, the discrepancy between the real and predicted values is computed as

$$L_1 = \frac{1}{M}\sum_{i=1}^{M}(V_{S,i}^{\mathrm{real}} - V_{S,i}^{\mathrm{pre}})^2, \tag{2}$$

where $V_{S,i}^{\mathrm{real}}$ is the ith sample point of the S-wave velocity as the ground truth, $V_{S,i}^{\mathrm{pre}}$ is the value estimated by DNN at the ith sample point, and M is the number of samples.

Similarly, the deviation between the RPM and DNN prediction values is calculated as

$$L_2 = \frac{1}{M}\sum_{i=1}^{M}(V_{S,i}^{\mathrm{RPM}} - V_{S,i}^{\mathrm{pre}})^2, \tag{3}$$

where $V_{S,i}^{\mathrm{RPM}}$ is the value estimated by the RPM.

Thus, the total loss function is

$$\mathrm{Loss} = \lambda_1 L_1 + \lambda_2 L_2, \tag{4}$$

where λ_1 and λ_2 are the weight factors, which we set equal to one.

Data normalization and evaluation metrics

Data normalization is a critical preprocessing step, as the input features often vary significantly in scale and units, which can adversely affect the performance of activation functions and the overall training process. Normalization not only ensures consistent scaling but also accelerates the convergence of the model. Given the input data set $\mathbf{X}$, the maximum and minimum values ($x_i^{\max}$ and $x_i^{\min}$), respectively) for each feature can be determined. Alternatively, normalization can be performed by using the mean and standard deviation of the training data. In this study, each feature x_i is normalized to the range [−1, 1] with

$$x_i^{\mathrm{norm}} = -1 + \frac{2}{x_i^{\max} - x_i^{\min}}(x_i - x_i^{\min}). \quad (5)$$

The accuracy of the predictions is measured by calculating the average squared differences between the observed and predicted values (root-mean-square error [RMSE]) and the proportion of variability explained by the model (R^2), given by

$$\mathrm{RMSE} = \sqrt{\frac{1}{n}\sum_{i=1}^{n}(y_i - y_{p,i})^2}, \quad (6)$$

$$R^2 = 1 - \sum_{i=1}^{n}(y_i - y_{p,i})^2 \Big/ \sum_{i=1}^{n}(y_i - \bar{y})^2, \quad (7)$$

where n is the number of samples; y_i and $y_{p,i}$ are the actual and predicted values, respectively; and $\bar{y} = \sum_{i=1}^{n} y_i/n$.

RESULTS

Input feature selection

In this section, five combinations of log parameters, (V_P), (V_P, ρ), (V_P, ρ, ϕ), (V_P, ρ, ϕ, Vcl), and (V_P, ρ, ϕ, Vcl, S_w), are evaluated to identify the most effective input features. For training the DNN-based V_S prediction model, a data set comprising 7989 data points from two wells (3729 and 4260 from wells 1 and 2, respectively) is used. The data points from wells 3 to 5 (3562, 4089, and 3941 from wells 3, 4, and 5, respectively) are used to validate the DNN model's performance and evaluate its prediction accuracy. A fully connected network architecture is adopted, consisting of five hidden layers, each containing 30 nodes. The tanh function is the activation function, and the Adam optimizer is used with an initial learning rate set to 0.001. The learning rate decay is achieved through the "lr_scheduler" in PyTorch, which dynamically modifies the learning rate according to the epoch count. This strategy helps stabilize the loss function minimization process by reducing fluctuations in the loss curve. During optimization, the DNN parameters are continuously refined to achieve a lower loss value.

The loss value is shown in Figure 6a. As can be seen, the training loss gradually decreases and reaches its lowest point after 10,000 epochs. The RMSE is computed for all predicted data. According to Figure 6b and Table 1, increasing the number of inputs in the V_S prediction NN enhances prediction accuracy. Therefore, the subsequent sections of this work will use five inputs (V_P, ρ, ϕ, Vcl, and S_w) to train the NN.

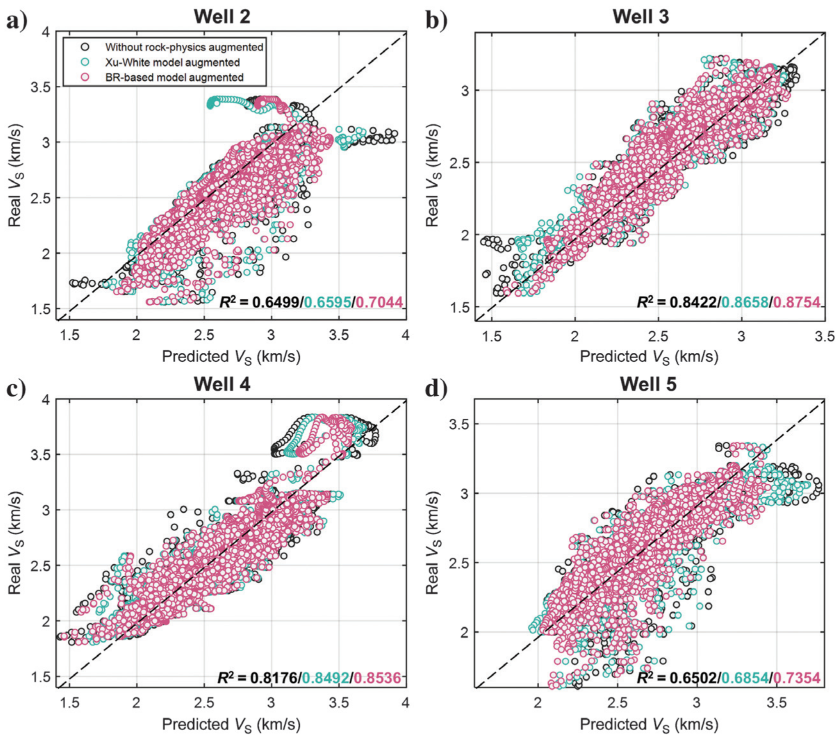

Figure 13. Crossplots of the real and predicted V_S using the Xu-White and BR models for well 1 training: (a) well 2, (b) well 3, (c) well 4, and (d) well 5.

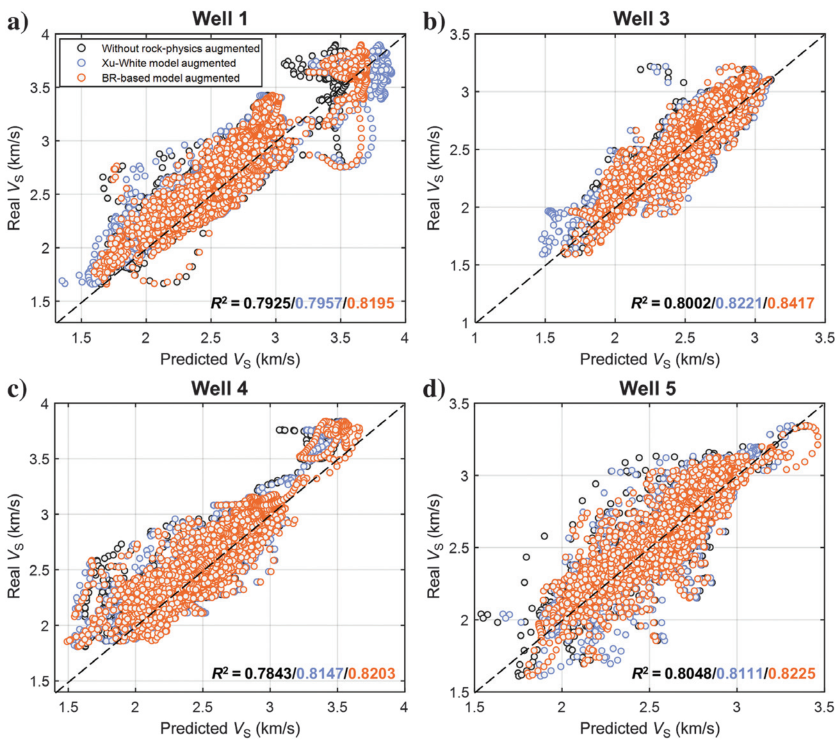

Figure 14. The same as Figure 13, but for well 2 with (a) well 1, (b) well 3, (c) well 4, and (d) well 5.

Testing RPMs and the generation of pseudolabels

Before creating pseudolabels with rock physics, we test the performance of predicting the V_P and V_S of wells 1–5. Table 2 shows the properties for the tests. The matrix is a mixture of quartz, clay, and feldspar minerals, and the feldspar content is low, with the ratio of feldspar to quartz being approximately 3% (Li et al., 2022). The comparison of the actual log data (the black curves), the estimated V_P and V_S obtained with the Xu-White model (the light green curves), and the BR model (the orange curves) is shown in Figure 7. The predictions of the BR model show a higher degree of agreement with the real log data.

Next, the pseudolabel data set for training is created by a Monte Carlo method, by assuming that the key parameters (ρ, ϕ, Vcl, and S_w) are statistically independent. Each parameter is considered to follow a uniform distribution within a specified range, and random sampling is performed within this parameter space to derive the potential combinations of these parameters. The main difficulty in calculating the wave velocities with the BR model is determining the inclusion volume, which has a correlation with the clay volume (Guo et al., 2022). Therefore, we statistically analyze this correlation in wells 1–5 (Figure 8) and derive an empirical relationship. Based on that, the inclusion volume of the synthetic data is calculated. Subsequently, the V_P and V_S are determined using the Xu-White and BR models. Table 3 shows the sampling ranges for the rock properties obtained from the actual data.

To ascertain the required number of pseudolabel data points for training, various training sets are created through random sampling with differing sample sizes. Six DNN models are trained with 0, 1000, 2000, 3000, 4000, and 5000 pseudolabel data points added to well 1. The data points of wells 2–5 are used to check the performance of the DNN model and analyze the prediction accuracy. As shown in Figure 9, the accuracy is relatively low when the number of pseudolabels is small, and then increases when it reaches a value of 2000. Figure 10 shows the V_P and V_S (Figure 10f and 10g) obtained with the Xu-White model and the BR model, respectively, for 2000 synthetic data points.

Table 4. The relative RMSE and R^2 between the real data and the prediction results in Figure 11.

Well	Training data	Relative RMSE	R^2
2	Without models	0.0745	0.6499
3		0.0478	0.8422
4		0.0613	0.8176
5		0.0670	0.6502
2	Xu-White model	0.0734	0.6595
3		0.0441	0.8658
4		0.0557	0.8492
5		0.0636	0.6854
2	BR model	0.0684	0.7044
3		0.0425	0.8754
4		0.0549	0.8536
5		0.0583	0.7354

Table 5. The relative RMSE and R^2 between the real data and the prediction results in Figure 12.

Well	Training data	Relative RMSE	R^2
1	Without models	0.0733	0.7925
3		0.0538	0.8002
4		0.0667	0.7843
5		0.0500	0.8048
1	Xu-White model	0.0727	0.7957
3		0.0507	0.8221
4		0.0618	0.8147
5		0.0493	0.8111
1	BR model	0.0684	0.8195
3		0.0479	0.8417
4		0.0608	0.8203
5		0.0477	0.8225

Table 6. Sampling ranges for the rock properties.

Property	Symbol (unit)	Lower bound	Upper bound
Density	ρ (g/cm^3)	2	3
Porosity	ϕ (v/v)	0.001	0.15
Clay volume	Vcl (v/v)	0.01	0.99
Water saturation	S_w (v/v)	0.01	0.99

Evaluation of RPM combinations

In this section, we investigate the effects of different RPMs on the prediction accuracy of V_S. Our goal is to improve the understanding of DNN-based predictions, especially in scenarios with limited labeled data. To validate the effectiveness of our proposed RPM-driven DNN strategies, we train the DNN model with data from one well and perform blind tests with the remaining four wells.

As shown in Figures 11 and 12, we take wells 1 and 2 as the cases to evaluate the prediction results of the blind wells using the Xu-White (the dotted line) and the BR (the dashed line) models. It can be seen that the prediction has been improved by using these models, especially in areas where the error is high without models (e.g., Figure 11b at the depths of 3460–3535 m and 3575–3630 m). Comparing the areas indicated by the dashed orange boxes in Figures 11 and 12, it is shown that the DNN model driven by the BR model outperforms the performance driven by the Xu-White model in terms of prediction accuracy at locations with larger errors. Compared with the Xu-White model, the BR model captures more physical information about the target layer, providing a better representation of the heterogeneity caused by pore structures in tight sandstone reservoirs. Furthermore, in rock-physics modeling, the spatial variability of the inclusion content associated with microcracks is considered, enabling the RPM to better characterize in situ pore structures.

Figures 13 and 14 show crossplots of the real and predicted results of four wells. The black dots represent the results predicted without rock physics, the dark green and light blue dots represent the results predicted with the Xu-White model, and the pink and orange dots represent those of the BR model. In addition, as indicated in the lower right corner of Figures 13 and 14, we compare the R^2 between the actual and predicted values with and without RPMs. It can be seen that the RPM-driven DNN model improves the prediction performance, especially for the BR-DNN model, with R^2 increasing from 0.6499 to 0.7044 for well 2, from 0.8422 to 0.8754 for well 3, from 0.8176 to 0.8536 for well 4, and from 0.6502 to 0.7354 for well 5 in the case of training well 1. Similarly, R^2 is increased from 0.7925 to 0.8195 for well 1, from 0.8002 to 0.8417 for well 3, from 0.7843 to 0.8203 for well 4, and from 0.8048 to 0.8225 for well 5 in the case of training for well 2.

Tables 4 and 5 provide the relative RMSE and R^2 between the real log data and the prediction results for the three DNN-based models. It can be seen that the BR-DNN results match the ground truth well. Especially when we use well 1 as the training data to predict well 5, the relative RMSE is decreased by approximately 13%.

General applicability of the proposed DNN method

To illustrate the potential applicability of the proposed method, data from a tight oil sandstone reservoir are used to train the neural network. The data set is from the Changqing oil field in the Ordos Basin. It is comprised of 2570 data points with V_P, V_S, ρ, ϕ, Vcl, and S_w.

The data set is comprised of three wells, labeled A, B, and C. To assess the effectiveness of the methodology, we select wells B and C as the test data set. Well A, with 1243 data points, is used to train the NN model as real labels. Subsequently, the pseudolabel data set used for training is generated by a Monte Carlo approach. After testing, a total of 500 pseudolabel data points are generated. Table 6 shows the sample ranges for the rock properties obtained in wells A–C. Subsequently, V_P and V_S are determined using the Xu-White and BR models, respectively.

The results are shown in Figure 15. It can be observed that when the Xu-White and BR models are considered for well A, the results are in better agreement with the log data. Table 7 shows the relative RMSE and R^2 of the V_S predictions for the three DNN-based models. Compared with the DNN model without modes, the DNN with the Xu-White model shows no significant improvement in prediction accuracy for well B but reduces the relative RMSE for well C by approximately 17.5%. In contrast, the BR model reduces the relative RMSE for wells B and C by approximately 12.1% and 19.7%, respectively. As shown in Figure 16, the results obtained with the BR model show a stronger correlation with the actual data, as most data points are predominantly close to the standard line. Although the previous examples focus primarily on a tight gas-sandstone reservoir, the case presented in this section shows that the proposed method is also applicable to tight oil-sandstone reservoirs. These cases demonstrate that the methodology presented here offers accuracy and generalizability.

DISCUSSION

Because RPMs are imperfect, inaccurate pseudolabels could affect the performance of the DNN model. Therefore, based on the two sets of pseudolabels in Figure 10, we sequentially add 5%,

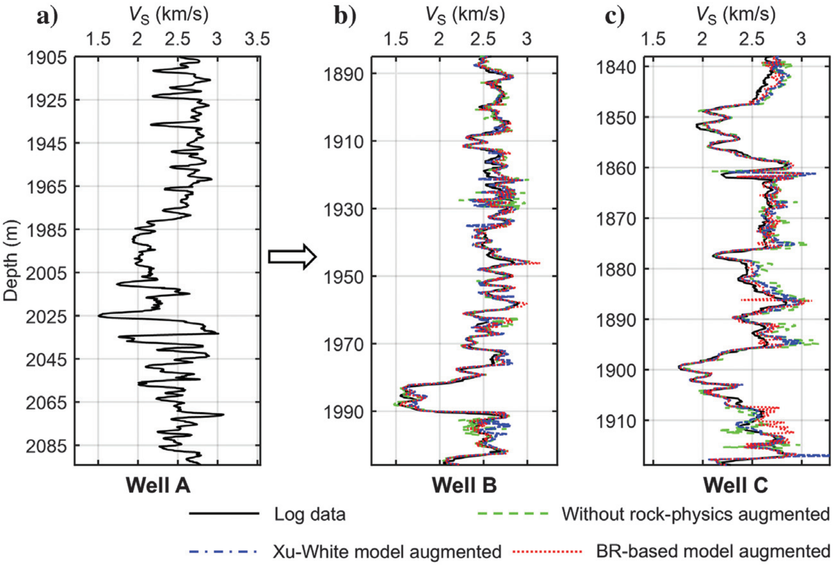

Figure 15. Comparisons of the DNN test results for V_S prediction by using the Xu-White and BR models for well A training.

Table 7. The relative RMSE and R^2 between the real data and the prediction results in Figure 15.

Well	Training data	Relative RMSE	R^2
B	Without rock-physics driven	0.0423	0.8537
C		0.0645	0.5901
B	Xu-White model driven	0.0420	0.8554
C		0.0532	0.7214
B	BR model driven	0.0372	0.8864
C		0.0518	0.7362

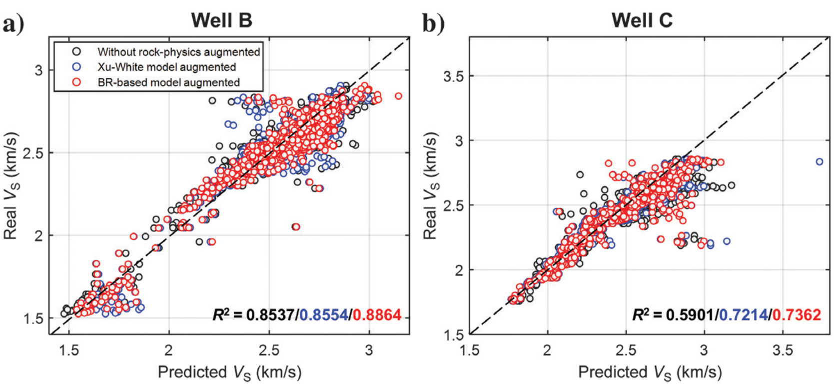

Figure 16. Crossplots of the real and predicted V_S by using the Xu-White and BR models for well A training: (a) well B and (b) well C.

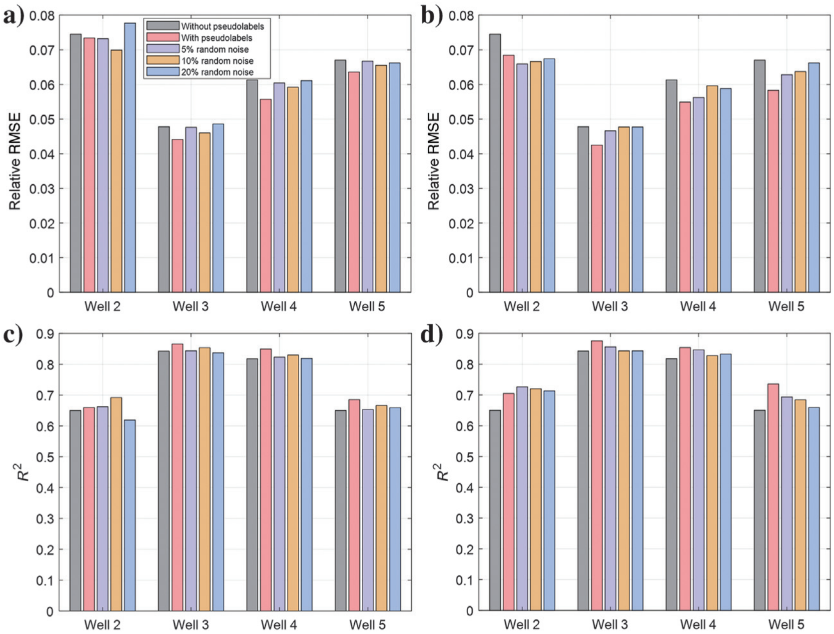

Figure 17. (a and b) The relative RMSE and (c and d) R^2 values for blind well predictions using pseudolabels with added random noise for (a and c) for Xu-White model and (b and d) the BR-based model augmented DNN, respectively.

10%, and 20% random noise to each set and insert them into the training data of well 1 to train the DNN model. The model is then validated using blind tests in wells 2–4, where the corresponding relative RMSE and R^2 values were calculated. The results are shown in Figure 17 (where Figure 17a and 17c shows the results based on the Xu-White model, whereas Figure 17b and 17d shows the results based on the BR model). Figure 17 shows that the inclusion of pseudolabels decreases the relative RMSE and increases the R^2 value in blind hole predictions, thereby improving the prediction accuracy. Although the introduction of random noise generally worsens prediction performance, the results are still better than those of the DNN models trained without pseudolabels. This indicates that, despite potential shortcomings in the RPMs, the pseudolabels derived within acceptable error margins can improve the predictive capability of the DNN model to a certain extent. A comparison of Figure 17a and 17c with 17b and 17d shows that the pseudolabels generated from the BR model generally provide better blind hole predictions, with and without random noise, than those derived from the Xu-White model. Therefore, it is more important to select an appropriate model to characterize reservoir properties, as it can provide pseudolabels with richer information about reservoir characteristics.

Although the current study shows that a pretrained model can be adapted to a new region by fine tuning it with limited well data, this process is more akin to transfer learning than a true generalization of the original model. This distinction is important because a true generalization would imply robust performance across multiple regions without retraining, whereas transfer learning explicitly uses prior knowledge while adapting to new data. However, this work primarily focuses on investigating how more accurate pseudolabels generated from RPMs affect the performance of DNN models under limited real data conditions, while validating their applicability in different study areas. Although advanced transfer learning techniques (e.g., domain adaptation, layer freezing, or feature-space alignment) were not investigated here, they represent a promising way to improve model performance, especially in cases where there are limited labeled data for the target domain. Future work should systematically evaluate these methods to further improve the adaptability of the model to different geologic settings.

CONCLUSION

A methodology for RPM-driven DNNs is proposed to predict S-wave velocity in tight sandstone reservoirs from logging data, by using density, porosity, clay volume, water saturation, and P-wave velocity. Our framework combines two RPMs, namely, the Xu-White and BR models. In particular, the variation of the inclusion volume with depth is considered to describe complex porous structures in the BR modeling. These RPMs are used to generate pseudolabels and construct a rock-physics-related loss function. The proposed method is validated in the tight-gas sandstone reservoirs of the Ordos Basin by training the DNN model with data from a single well and evaluating its performance with data from the other four wells. We find that both RPM-driven DNN approaches effectively improve prediction accuracy. The combination of the BR model with the rock-physics pseudolabeling strategy shows good improvements, reducing the relative RMSE by up to 13%. Moreover, the predictions in different regions and reservoirs show that the proposed method has generalization capabilities and provides a technical framework for supporting the evaluation of sweet spots in tight reservoirs. Future work will extend this DNN-based method to process data from carbon storage and geothermal reservoirs.

ACKNOWLEDGMENTS

This work was supported by the National Natural Science Foundation of China (42174161 and 42404128), the Fundamental Research Funds for the Central Universities (B240205030), the Natural Science Foundation of Jiangsu Province (BK20220995), and the China Scholarship Council (202406710107).

DATA AND MATERIALS AVAILABILITY

Data associated with this research are available and can be obtained by contacting the corresponding author.

APPENDIX A

THE BR EQUATION AND ITS PLANE-WAVE SOLUTION

To describe wave propagation in a double-porosity medium, Ba et al. (2011) propose the BR model. The governing equations are

$$N\nabla^2\mathbf{u} + (A+N)\nabla\varepsilon + Q_1(\zeta^{(1)} + \phi_2\varsigma) + Q_2(\zeta^{(2)} - \phi_1\varsigma) = \rho_{11}\ddot{\mathbf{u}} + \rho_{12}\ddot{\mathbf{U}}^{(1)} + \rho_{13}\ddot{\mathbf{U}}^{(2)} + b_1(\dot{\mathbf{u}} - \dot{\mathbf{U}}^{(1)}) + b_2(\dot{\mathbf{u}} - \dot{\mathbf{U}}^{(2)}), \quad \text{(A-1)}$$

$$Q_1\nabla\varepsilon + R_1\nabla(\zeta^{(1)} + \phi_2\varsigma) = \rho_{12}\ddot{\mathbf{u}} + \rho_{22}\ddot{\mathbf{U}}^{(1)} - b_1(\dot{\mathbf{u}} - \dot{\mathbf{U}}^{(1)}), \quad \text{(A-2)}$$

$$Q_2\nabla\varepsilon + R_2\nabla(\zeta^{(2)} - \phi_1\varsigma) = \rho_{13}\ddot{\mathbf{u}} + \rho_{33}\ddot{\mathbf{U}}^{(1)} - b_2(\dot{\mathbf{u}} - \dot{\mathbf{U}}^{(2)}), \quad \text{(A-3)}$$

$$\phi_2(Q_1\varepsilon + R_1(\zeta^{(1)} + \phi_2\varsigma)) - \phi_1(Q_2\varepsilon + R_2(\zeta^{(2)} - \phi_1\varsigma)) = \frac{1}{3}\rho_f\ddot{\varsigma}R_0^2\frac{\phi_1^2\phi_2\phi_{20}}{\phi_{10}} + \frac{1}{3}\frac{\eta\phi_1^2\phi_2\phi_{20}}{\kappa_1}\dot{\varsigma}R_0^2, \quad \text{(A-4)}$$

where $\mathbf{u}$ denotes the displacement vector of the dry rock skeleton, whereas $\mathbf{U}^{(1)}$ and $\mathbf{U}^{(2)}$ correspond to the average fluid displacement vectors of the host and inclusions, respectively. The terms ε, $\zeta^{(1)}$, and $\zeta^{(2)}$ describe three divergence fields associated with displacement. The scalar ζ represents the fluid change resulting from fluid flow. The absolute porosities of the host and inclusion are denoted by ϕ_1 and ϕ_2, respectively. Here, κ_1, η, and R_0 represent the permeability of the host medium, the fluid viscosity, and the radius of inclusions, respectively. The equations include two Biot dissipation coefficients (b_1 and b_2), six stiffness parameters (A, N, Q_1, R_1, Q_2, R_2), and five density coefficients (ρ_{11}, ρ_{12}, ρ_{13}, ρ_{22}, ρ_{33}).

By using the plane-wave kernel in equations A-1–A-4, the equation governing P waves can be expressed as

$$\begin{vmatrix} a_{11}k^2 + b_{11} & a_{12}k^2 + b_{12} & a_{13}k^2 + b_{13} \\ a_{21}k^2 + b_{21} & a_{22}k^2 + b_{22} & a_{23}k^2 + b_{23} \\ a_{31}k^2 + b_{31} & a_{32}k^2 + b_{32} & a_{33}k^2 + b_{33} \end{vmatrix} = 0, \quad \text{(A-5)}$$

with

$$\begin{aligned} a_{11} &= A + 2N + i(Q_2\phi_1 - Q_1\phi_2)x_1, \\ b_{11} &= -\rho_{11}\omega^2 + i\omega(b_1 + b_2), \\ a_{12} &= Q_1 + i(Q_2\phi_1 - Q_1\phi_2)x_2, \quad b_{12} = -\rho_{12}\omega^2 - i\omega b_1, \\ a_{13} &= Q_2 + i(Q_2\phi_1 - Q_1\phi_2)x_3, \quad b_{13} = -\rho_{13}\omega^2 - i\omega b_2, \\ a_{21} &= Q_1 - iR_1\phi_2x_3, \quad b_{21} = -\rho_{12}\omega^2 - i\omega b_1, \\ a_{22} &= R_1 - iR_1\phi_2x_2, \quad b_{22} = -\rho_{22}\omega^2 + i\omega b_1, \\ a_{23} &= -iR_1\phi_2x_3, \quad b_{23} = 0, \\ a_{31} &= Q_2 + iR_2\phi_1x_1, \quad b_{31} = -\rho_{13}\omega^2 - i\omega b_2, \\ a_{32} &= iR_2\phi_1x_2, \quad b_{32} = 0, \\ a_{33} &= R_2 + iR_2\phi_1x_3, \quad b_{33} = -\rho_{33}\omega^2 + i\omega b_2, \end{aligned} \quad \text{(A-6)}$$

and

$$x_1 = \frac{i(\phi_2Q_1 - \phi_1Q_2)}{Z}, \quad x_2 = \frac{i\phi_2R_1}{Z}, \quad x_3 = -\frac{i\phi_1R_2}{Z},$$
$$Z = \frac{i\omega\eta\phi_1^2\phi_2\phi_{20}R_0^2}{3\kappa_1} - \frac{\rho_f\omega^2R_0^2\phi_1^2\phi_2\phi_{20}}{3\phi_{10}} - (\phi_2^2R_1 + \phi_1^2R_2). \quad \text{(A-7)}$$

The phase velocity is (Carcione, 2022)

$$V_P = \left[\mathrm{Re}\left(\frac{k}{\omega}\right)\right]^{-1}, \quad \text{(A-8)}$$

where k and ω are the complex wavenumber and the angular frequency, respectively.

REFERENCES

Agofack, N., S. Lozovyi, and A. Bauer, 2018, Effect of CO2 on P- and S-wave velocities at seismic and ultrasonic frequencies: International Journal of Greenhouse Gas Control, **78**, 388–399, doi: 10.1016/j.ijggc.2018.09.010.

Ajo-Franklin, J. B., J. Peterson, J. Doetsch, and T. M. Daley, 2013, High-resolution characterization of a CO2 plume using crosswell seismic tomography: Cranfield, MS, USA: International Journal of Greenhouse Gas Control, **18**, 497–509, doi: 10.1016/j.ijggc.2012.12.018.

Anemangely, M., A. Ramezanzadeh, H. Amiri, and S.-A. Hoseinpour, 2019, Machine learning technique for the prediction of shear wave velocity using petrophysical logs: Journal of Petroleum Science and Engineering, **174**, 306–327, doi: 10.1016/j.petrol.2018.11.032.

Anemangely, M., A. Ramezanzadeh, and B. Tokhmechi, 2017, Shear wave travel time estimation from petrophysical logs using ANFIS-PSO algorithm: A case study from Ab-Teymour Oilfield: Journal of Natural Gas Science and Engineering, **38**, 373–387, doi: 10.1016/j.jngse.2017.01.003.

Ba, J., J. M. Carcione, and J. X. Nie, 2011, Biot-Rayleigh theory of wave propagation in double-porosity media: Journal of Geophysical Research: Solid Earth, **116**, B06202, doi: 10.1029/2010JB008185.

Ba, J., Z. J. Fang, L.-Y. Fu, W. H. Xu, and L. Zhang, 2023a, Acoustic wave propagation in a porous medium saturated with a Kelvin-Voigt non-Newtonian fluid: Geophysical Journal International, **235**, 2056–2077, doi: 10.1093/gji/ggad355.

Ba, J., R. P. Ma, J. M. Carcione, Y. Shi, and L. Zhang, 2023b, Effects of pore geometry and saturation on the behavior of multiscale waves in tight sandstone layers: Journal of Geophysical Research: Solid Earth, **128**, e2023JB027542, doi: 10.1029/2023JB027542.

Ba, J., W. H. Xu, L.-Y. Fu, J. M. Carcione, and L. Zhang, 2017, Rock anelasticity due to patchy saturation and fabric heterogeneity: A double double-porosity model of wave propagation: Journal of Geophysical Research: Solid Earth, **122**, 1949–1976, doi: 10.1002/2016JB013882.

Bagheripour, P., A. Gholami, M. Asoodeh, and M. Vaezzadeh-Asadi, 2015, Support vector regression based determination of shear wave velocity: Journal of Petroleum Science and Engineering, **125**, 95–99, doi: 10.1016/j.petrol.2014.11.025.

Brantut, N., and P. Baud, 2025, Development of permeability heterogeneity during compaction of porous sandstone: Journal of Geophysical Research: Solid Earth, **130**, e2024JB030022, doi: 10.1029/2024JB030022.

Carcione, J. M., 2022, Wave fields in real media. Theory and numerical simulation of wave propagation in anisotropic, anelastic, porous and electromagnetic media, 4rd ed.: Elsevier.

Carcione, J. M., H. B. Helle, and P. Avseth, 2011, Source-rock seismic-velocity models: Gassmann versus Backus: Geophysics, **76**, no. 5, N37–N45, doi: 10.1190/geo2010-0258.1.

Carcione, J. M., A. Q. Qadrouh, M. Alajmi, N. B. Alqahtani, and J. Ba, 2023, Rock acoustics of CO2 storage in basalt: Geophysical Journal International, **234**, 2429–2435, doi: 10.1093/gji/ggad252.

Dautriat, J., N. Gland, A. Dimanov, and J. Raphanel, 2011, Hydromechanical behavior of heterogeneous carbonate rock under proportional triaxial loadings: Journal of Geophysical Research: Solid Earth, **116**, B01205, doi: 10.1029/2009JB000830.

Dumke, I., and C. Berndt, 2019, Prediction of seismic P-wave velocity using machine learning: Solid Earth, **10**, 1989–2000, doi: 10.5194/se-10-1989-2019.

Evro, S., B. A. Oni, and O. S. Tomomewo, 2025, Repurposing depleted unconventional reservoirs for hydrogen storage: Challenges and opportu-

nities: International Journal of Hydrogen Energy, **99**, 53–68, doi: 10.1016/j.ijhydene.2024.12.212.
Fang, Z. J., J. Ba, J. M. Carcione, W. S. Liu, and C. S. Wang, 2022, Estimation of the shear-wave velocity of shale-oil reservoirs: A case study of the Chang 7 Member in the Ordos Basin: Journal Seismic Exploration, **31**, 81–104.
Fang, Z. J., J. Ba, Q. Guo, and F. S. Xiong, 2024, Shear-wave velocity prediction of tight reservoirs based on poroelasticity theory: A comparative study of deep neural network and rock physics model: Geoenergy Science and Engineering, **240**, 213028, doi: 10.1016/j.geoen.2024.213028.
Feng, G., Z. Yang, X. R. Xu, W. Yang, and H. H. Zeng, 2024, Shear wave velocity prediction for fractured limestone reservoirs based on artificial neural network: Geophysical Prospecting, **72**, 2646–2665, doi: 10.1111/1365-2478.13550.
Gassmann, F., 1951, Uber die elastic poroser media: Vierteljahrschrift der Naturforschenden Gesellschaft in Zürich, **96**, 1–23.
Gu, Y. F., Z. D. Bao, X. M. Song, M. Y. Wei, D. S. Zang, B. Niu, and K. Lu, 2019, Permeability prediction for carbonate reservoir using a data-driven model comprising deep learning network, particle swarm optimization, and support vector regression: A case study of the LULA oilfield: Arabian Journal of Geosciences, **12**, 622, doi: 10.1007/s12517-019-4804-3.
Guo, J. X., X. F. Chen, J. G. Zhan, and Z. J. Xiao, 2024, Effects of background elastic and permeability anisotropy on dynamic seismic signatures of a fluid-saturated porous rock with aligned fractures: Geophysics, **89**, no. 6, MR335–MR354, doi: 10.1190/geo2024-0377.1.
Guo, J. X., and B. Y. Fu, 2024, Effective elastic properties of fractured rocks considering fracture interactions: Geophysical Prospecting, **73**, 330–344, doi: 10.1111/1365-2478.13632.
Guo, Q., J. Ba, and J. M. Carcione, 2022, Multi-objective petrophysical seismic inversion based on the double-porosity Biot–Rayleigh model: Surveys in Geophysics, **43**, 1117–1141, doi: 10.1007/s10712-022-09692-6.
Guo, Z. Q., and X. Y. Li, 2015, Rock physics model-based prediction of shear wave velocity in the Barnett Shale formation: Journal of Geophysics and Engineering, **12**, 527–534, doi: 10.1088/1742-2132/12/3/527.
Han, D.-H., A. Nur, and D. Morgan, 1986, Effects of porosity and clay content on wave velocities in sandstones: Geophysics, **51**, 2093–2107, doi: 10.1190/1.1442062.
Ivanova, A., A. Kashubin, N. Juhojuntti, J. Kummerow, J. Henninges, C. Juhlin, S. Lüth, and M. Ivandic, 2012, Monitoring and volumetric estimation of injected CO2 using 4D seismic, petrophysical data, core measurements and well logging: A case study at Ketzin, Germany: Geophysical Prospecting, **60**, 957–973, doi: 10.1111/j.1365-2478.2012.01045.x.
Jia, C. Z., X. Q. Pang, and Y. Song, 2023, Whole petroleum system and ordered distribution pattern of conventional and unconventional oil and gas reservoirs: Petroleum Science, **20**, 1–19, doi: 10.1016/j.petsci.2022.12.012.
Jiang, R., Z. F. Ji, W. L. Mo, S. H. Wang, M. J. Zhang, W. Yin, Z. Wang, Y. P. Lin, X. K. Wang, and U. Ashraf, 2022, A novel method of deep learning for shear velocity prediction in a tight sandstone reservoir: Energies, **15**, 7016, doi: 10.3390/en15197016.
Kadkhodaie, A., and R. Kadkhodaie, 2022, Reservoir characterization of tight gas sandstones: Exploration and development: Elsevier.
Khalilidermani, M., and D. Knez, 2024, Shear wave velocity applications in geomechanics with focus on risk assessment in carbon capture and storage projects: Energies, **17**, 1578, doi: 10.3390/en17071578.
Khatiwada, M., L. Adam, M. Morrison, and K. Wijk, 2013, A feasibility study of time-lapse seismic monitoring of CO2 sequestration in a layered basalt reservoir: Journal of Applied Geophysics, **82**, 145–152, doi: 10.1016/j.jappgeo.2012.03.005.
Kim, J., T. Matsuoka, and Z. Q. Xue, 2011, Monitoring and detecting CO2 injected into water-saturated sandstone with joint seismic and resistivity measurements: Exploration Geophysics, **42**, 58–68, doi: 10.1071/EG11002.
Kocoglu, Y., S. B. Gorell, H. Emadi, D. S. Eyinla, F. Bolouri, Y. C. Kocoglu, and A. Arora, 2024, Improving the accuracy of short-term multiphase production forecasts in unconventional tight oil reservoirs using contextual bi-directional long short-term memory: Geoenergy Science and Engineering, **235**, 212688, doi: 10.1016/j.geoen.2024.212688.
Lee, M. W., 2006, A simple method of predicting S-wave velocity: Geophysics, **71**, no. 6, F161–F164, doi: 10.1190/1.2357833.
Li, C., P. Hu, J. Ba, J. M. Carcione, T. W. Hu, and M. Q. Pang, 2022, Seismic estimation of fluid saturation based on rock physics: A case study of the tight-gas sandstone reservoirs in the Ordos Basin: Interpretation, **10**, no. 1, SA35–SA46, doi: 10.1190/INT-2021-0124.1.
Li, Y. E., D. O'Malley, G. Beroza, A. Curtis, and P. Johnson, 2023, Machine learning developments and applications in solid-earth geosciences: Fad or future? Journal of Geophysical Research: Solid Earth, **128**, e2022JB026310, doi: 10.1029/2022JB026310.
Mavko, G., T. Mukerji, and J. Dvorkin, 2020, The rock physics handbook: Cambridge University Press.
Oloruntobi, O., and S. Butt, 2020, The shear-wave velocity prediction for sedimentary rocks: Journal of Natural Gas Science and Engineering, **76**, 103084, doi: 10.1016/j.jngse.2019.103084.
Pan, H. J., C. Wei, X. F. Yan, X. M. Li, Z. F. Yang, Z. X. Gui, and S. X. Liu, 2024, 3D rock physics template-based probabilistic estimation of tight sandstone reservoir properties: Petroleum Science, **21**, 3090–3101, doi: 10.1016/j.petsci.2024.04.010.
Qadrouh, A. N., J. M. Carcione, M. Alajmi, and M. M. Alyousif, 2019, A tutorial on machine learning with geophysical applications: Bollettino di Geofisica Teorica ed Applicate, **60**, 375–402.
Qin, X., L. X. Zhao, Z. J. Cai, Y. Wang, M. H. Xu, F. S. Zhang, D. H. Han, and J. H. Geng, 2022, Compressional and shear wave velocities relationship in anisotropic organic shales: Journal of Petroleum Science and Engineering, **219**, 111070, doi: 10.1016/j.petrol.2022.111070.
Rajabi, M., B. Bohloli, and E. Gholampour Ahangar, 2010, Intelligent approaches for prediction of compressional, shear and Stoneley wave velocities from conventional well log data: A case study from the Sarvak carbonate reservoir in the Abadan Plain (Southwestern Iran): Computers & Geosciences, **36**, 647–664, doi: 10.1016/j.cageo.2009.09.008.
Rezaee, M. R., A. Kadkhodaie-Ilkhchi, and A. Barabasi, 2007, Prediction of Vs from petrophysical data utilizing intelligent systems: An example from a sandstone reservoir of Carnarvon Basin, Australia: Journal of Petroleum Science and Engineering, **55**, 201–212, doi: 10.1016/j.petrol.2006.08.008.
Sambo, C., N. Liu, R. Shaibu, A. A. Ahmed, and R. G. Hashish, 2023, A technical review of CO2 for enhanced oil recovery in unconventional oil reservoirs: Geoenergy Science and Engineering, **221**, 111185, doi: 10.1016/j.petrol.2022.111185.
Singh, S. K., P. K. Chaudhuri, and A. K. Tandon, 2015, Machine learning tools and shear velocity prediction using conventional logs: An alternative approach: 11th Biennial International Conference Exposition.
Wang, J., and J. X. Cao, 2021, Data-driven S-wave velocity prediction method via a deep-learning-based deep convolutional gated recurrent unit fusion network: Geophysics, **86**, no. 6, M185–M196, doi: 10.1190/geo2020-0886.1.
Wang, J. L., S. G. Wu, L. X. Zhao, W. W. Wang, J. G. Wei, and J. Sun, 2019, An effective method for shear-wave velocity prediction in sandstones: Marine Geophysical Research, **40**, 655–664, doi: 10.1007/s11001-019-09396-4.
Wilkens, R., G. Simmons, and L. Caruso, 1984, The ratio Vp/Vs as a discriminant of composition for siliceous limestones: Geophysics, **49**, 1850–1860, doi: 10.1190/1.1441598.
Xiong, F. S., J. Ba, D. Gei, and J. M. Carcione, 2021, Data-driven design of wave propagation models for shale-oil reservoirs based on machine learning: Journal of Geophysical Research: Solid Earth, **126**, e2021JB022665, doi: 10.1029/2021JB022665.
Xu, S., and R. E. White, 1995, A new velocity model for clay-sand mixtures: Geophysical Prospecting, **43**, 91–118, doi: 10.1111/j.1365-2478.1995.tb00126.x.
Xu, S., and R. E. White, 1996, A physical model for shear wave velocity prediction: Geophysical Prospecting, **44**, 687–717, doi: 10.1111/j.1365-2478.1996.tb00170.x.
Yang, J. Q., N. T. Lin, K. Zhang, L. Y. Jia, and D. Zhang, 2023, An improved integration strategy for prediction of shear wave velocity using petrophysical logs: Integration of spatiotemporal and small sample nonlinear feature: Geoenergy Science and Engineering, **230**, 212270, doi: 10.1016/j.geoen.2023.212270.
You, N., Y. E. Li, and A. Cheng, 2020, Shale anisotropy model building based on deep neural networks: Journal of Geophysical Research: Solid Earth, **125**, e2019JB019042, doi: 10.1029/2019JB019042.
You, N., Y. E. Li, and A. Cheng, 2021, 3D carbonate digital rock reconstruction using progressive growing GAN: Journal of Geophysical Research: Solid Earth, **126**, e2021JB021687, doi: 10.1029/2021JB021687.
Zhang, D. X., Y. T. Chen, and J. Men, 2018, Synthetic well logs generation via recurrent neural networks: Petroleum Exploration and Development, **45**, 629–639, doi: 10.1016/S1876-3804(18)30068-5.
Zhang, Y. J., D. H. Wang, H. Li, and J. H. Gao, 2023, S-wave velocity prediction using physical model-driven Gaussian process regression: A case study of tight sandstone reservoir: Geophysics, **88**, no. 2, D85–D93, doi: 10.1190/geo2021-0708.1.
Zhao, L. X., C. H. Cao, Q. L. Yao, Y. R. Wang, H. Li, H. M. Yuan, J. H. Geng, and D. H. Han, 2020, Gassmann consistency for different inclusion-based effective medium theories: Implications for elastic interactions and poroelasticity: Journal of Geophysical Research: Solid Earth, **125**, e2019JB018328, doi: 10.1029/2019JB018328.
Zhao, L. X., J. Y. Liu, M. H. Xu, Z. Y. Zhu, Y. Y. Chen, and J. H. Geng, 2024, Rock-physics-guided machine learning for shear sonic log prediction: Geophysics, **89**, no. 1, D75–D87, doi: 10.1190/geo2023-0152.1.
Zou, C. F., L. X. Zhao, M. H. Xu, Y. Y. Chen, and J. H. Geng, 2021, Porosity prediction with uncertainty quantification from multiple seismic attributes using random forest: Journal of Geophysical Research: Solid Earth, **126**, e2021JB021826, doi: 10.1029/2021JB021826.
Zou, C. N., R. K. Zhu, K. Y. Liu, L. Su, B. Bai, X. X. Zhang, X. J. Yuan, and J. H. Wang, 2012, Tight gas sandstone reservoirs in China: Characteristics and recognition criteria: Journal of Petroleum Science and Engineering, **88–89**, 82–91, doi: 10.1016/j.petrol.2012.02.001.

Biographies and photographs of the authors are not available.